Journal of Sound and Vibration (2002) **252**(2), 343–360
doi:10.1006/jsvi.2001.4043, available online at http://www.idealibrary.com on IDEAL®

NON-DESTRUCTIVE EVALUATION OF HORIZONTAL CRACK DETECTION IN BEAMS USING TRANSVERSE IMPACT

S. I. Ishak, G. R. Liu, H. M. Shang and S. P. Lim

Department of Mechanical Engineering, National University of Singapore, 10 *Kent Ridge Crescent, Singapore* 119260. *E-mail*: *mpeliugr@nus.edu.sg*

(*Received* 14 *December* 2000, *and in final form* 17 *September* 2001)

Numerical and experimental studies for crack detection in beam employing transverse impact are presented. In the numerical study, a beam model of wave propagation is developed to calculate the time history of beam response before, over and after the crack region. It is expected that the resulting wave in the beam will be scattered by the crack and will carry information on the location and geometry of the crack. Experiments using a scanning laser vibrometer on specimens containing simulated crack are then conducted to verify the numerical results. Comparison study between the numerical results and experimental observations are conducted; good correlation between theory and experiment is observed. The beam model of wave propagation and adaptive multilayer perceptron networks (MLP) are then used for inverse identification of crack parameters (i.e., crack location, depth and length) in the beams. Time-domain displacement responses calculated using the present beam model containing predetermined crack parameters are used as training data for the MLP. Once the MLP is trained, the MLP networks are then employed for inverse determination of an unknown crack in a beam using experimental displacement responses measured with a scanning laser vibrometer. Examples show that the procedure performs well for the determination of a wide range of values for the location, depth and length of the crack.

1. INTRODUCTION

Cracks in metallic members and delaminations in laminated material are typical examples of flaws that are commonly found in beam structures. Many studies on the dynamics of flawed structural members have been reported. It has been reported [1–3] that the presence of a crack would alter the local flexibility of the structure at the flawed region, and subsequently lead to premature structural failure. The adverse effect on the dynamic behaviour of defects can be utilized as an effective means for identifying and assessing both the location and size of crack. Therefore, the development of appropriate methods for early crack detection becomes very important. Many reports on the dynamic behaviour of flawed structures have been published for the eventual purpose of developing the appropriate NDT tools; and the following is a brief review of recent theoretical and experimental studies.

Penn *et al.* [4] have used the free vibration method to detect delamination in thick composites. The vibration is initiated by a single mechanical impact and is sensed by surface-bonded piezoelectric film elements. Even though the method is attractive because of its simplicity, it is found that the method is relatively insensitive for detecting small-to-medium delaminations in plates. Springer *et al.* [5] have proposed a method based on the

0022-460X/02/$35.00

structural frequency response for non-destructive inspection of structural members; from the various numbers of experiments conducted, the technique is suitable for accurate determination of the location and size of damage.

In numerical analysis, Roche and Accorsi [6] have developed a new delaminated beam element for analyzing laminated beams containing delaminations. The advantage of the element is that it allows for modelling delaminations anywhere in the structure using a single finite element model. Results using the new element show good agreement with those obtained by constructing frame models using conventional laminated beam element. Using a simpler approach, Mujumdar *et al.* [7] proposed a new analytical model based on the Bernoulli–Euler beam theory. They assumed that at the flawed region, beam sections at both sides of the flaw are constrained to have identical transverse deformations and remain in contact throughout the vibration. The numerical results presented bring out the effects of flaw size, of its spanwise and thicknesswise location, of typical boundary conditions and of mode number on the frequencies and mode shapes. It was indicated that the predominant factors governing the extent of weakening produced by the flaw are the magnitude of shear force distribution and the average curvature of the beam over the delamination region.

The strip element method (SEM) has proven to be very efficient in detecting and locating the presence of a simple crack in materials [8, 9]. The primary concern with SEM is on the non-reflected boundary condition, which is used in the model in order to minimize reflection at the boundaries. However, in practical situations, this condition might not be easily satisfied; hence the need to explore other techniques that are independent of the boundary conditions.

One way is to excite the test structure with a transient force, and before the excitation wave can interfere with the wave that is reflected from the boundary of the structure, the response of the structure is recorded. Based on this principle, Doyle [10] used impact force and developed an inverse procedure combining the spectral element method and stochastic genetic algorithm to determine the size and location of crack in a beam. The method determines stiffness changes by using the formulations that relate the crack size to a single torsional stiffness parameter. Combined with the experimental results, this simple approach could indicate well the size and location of transverse cracks in beams. Prior to the work to determine the size and location of crack using impact force, Doyle and Kamle [11, 12] conducted a study of the transmission and reflection characteristics of flexural waves at structural discontinuities when a beam is impacted. Bernoulli–Euler beam model and a fast Fourier transform (FFT) algorithm are used to characterize the dispersive flexural waves. The results indicate that the presented model is adequate to track the wave as it passes through the joint, hence it can be used to describe structural discontinuities. Then, Doyle [13] used the frequency domain and the FFT analysis of the strain gauge measurements on an impacted plate to infer the contact force history. Using this approach, good estimates of the impact force on a composite plate can be obtained but to make the method more useful it is necessary to extend the solution for general anisotropic material. Doyle [14, 15] has also successfully used the phase information obtained from a spectral analysis of to determine the location and time of initiation of an unknown dispersing pulse.

Motivated by these observations, a beam model analyzing transverse impact-wave propagation in beams for the detection and assessment of cracks in beams are developed. In this model, beam responses are investigated and analyzed in time domain. The major advantage of beam model for solving the wave scattering problem is the much smaller number of equations compared with the FEM and even the SEM. Consequently, much shorter computing time is needed for solutions of comparable accuracy. The experimental study is later on conducted using laser vibrometer to verify the numerical results. Beam responses along its surface are observed for a very short interval of time before the

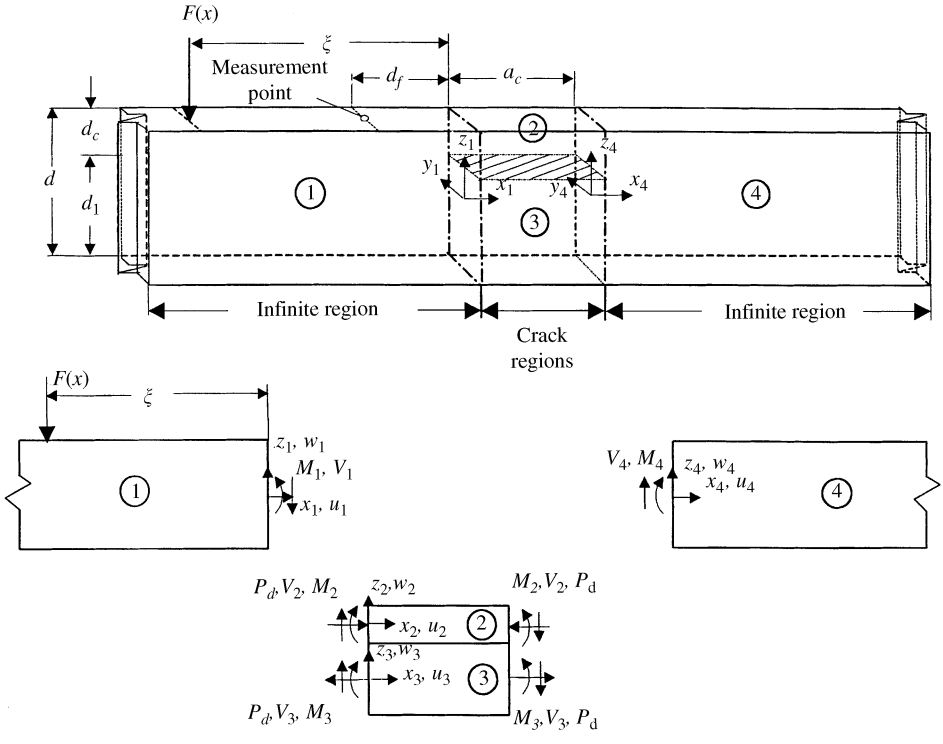

Figure 1. Geometry and modelling of a beam with a crack.

longitudinal wave is reflected by the boundary. Another numerical study by modelling a finite beam using finite element model (FEM) is developed by Chee [16]. Linear, two-dimensional, solid elements are used to create the model of flawless and flawed beams. The flaw in the beam is modelled as a slot, in which the nodes of the elements around the flaw are non-equivalence.

Comparison studies are then conducted between the beam model and laser measurements prior to the application of MLP network for inverse determination of crack in beams.

2. A BEAM MODEL OF FLEXURAL WAVE BY TRANSVERSE IMPACT

2.1. BASIC ASSUMPTIONS

In the present beam model of wave propagation, the beam is divided into four spanwise regions, namely two crack regions separated by the crack and two infinite regions one on each side of the crack regions, as shown in Figure 1. Each region is modelled as a Bernoulli–Euler beam.

The model is assumed as a thin beam and the effects of rotary inertia and shear deformation are not taken into consideration. Based on Bernoulli–Euler beam assumptions, this model can only be applied to beams in which the cross-sectional dimensions were small in comparison to its length. By not taking into account the effects of the cross-sectional dimensions on the frequencies and considering the actual beam cross-sectional dimensions in comparison to its length, the analysis will be limited to low-velocity impact force. The

solution for the entire cracked beam is obtained in terms of the solutions of all regions based on the theory of Bernoulli–Euler beam by satisfying the appropriate boundary conditions at the junctions between these regions.

The advantage of using infinite region in the present beam model is that the result can be compared to the experimental data with different boundary conditions at the time before the incidence wave is reflected.

2.2. HOMOGENEOUS SOLUTION OF BEAMS

The governing equation of motion for infinite regions free of external force can be presented as

$$\partial^4 w_i/\partial x_i^4 + (\rho A_{ci}/EI)\partial^2 w_i/\partial t^2 = 0, \quad i = 1, 4, \tag{1}$$

where I is the second moment of area of a beam region; ρ and E are the density and Young's modulus of the beam material. A_{ci}, x_i and w_i are the cross-sectional area, the axial co-ordinate and the transverse displacement of the region i. In the case of the cracked regions 2 and 3, the governing equations can be written as

$$-EI_2\,\partial^4 w_2/\partial x_2^4 - P_d\,\partial^2 w_2/\partial x_2^2 - \rho A_{c2}\,\partial^2 w_2/\partial t^2 - p = 0, \tag{2}$$

$$-EI_3\,\partial^4 w_3/\partial x^4 + P_d\,\partial^2 w_3/\partial x_3^2 - \rho A_{c3}\,\partial^2 w_3/\partial t^2 + p = 0, \tag{3}$$

where p is the normal contact pressure distribution between the two regions and P_d is the magnitude of the axial load in each region.

Regions 2 and 3 are set to have identical transverse displacements and they are assumed to be free to slide over each other in the axial direction except at their ends. At any section through the crack region ($x_2 = x_3$), w_2 is equal to w_3; by replacing w_3 and x_3 by w_2 and x_2 in equation (3), and adding it to equation (2), the governing equation can be written as

$$\partial^2 w_2/\partial x_2^4 + \{\rho(A_{c2} + A_{c3})/E(I_2 + I_3)\}\partial^2 w_2/\partial t^2 = 0. \tag{4}$$

For harmonic motion $w_{hi} = W_{hi}(x_i)\exp(\mathrm{i}\omega t)$, equation (4) can be written as

$$\partial^4 W_{hi}/\partial x_i^4 - \lambda_i^4 W_{hi} = 0, \quad i = 1, 2, 3, 4, \tag{5}$$

where the subscript h denotes the homogeneous solution, ω is the frequency, t is the time and λ_i are the frequency parameters. Considering the radiation condition at each region, the homogeneous solution for each region is given as

$$w_{hi}(x_i, t) = [A_i \exp(\mathrm{i}\lambda_i x_i) + C_i \exp(\lambda_i x_i)]\exp(\mathrm{i}\omega_i t), \quad i = 1, \tag{6a}$$

$$w_{hi}(x_i, t) = [A_i \exp(\mathrm{i}\lambda_i x_i) + B_i \exp(-\mathrm{i}\lambda_i x_i) + C_i \exp(\lambda_i x_i) + D_i \exp(-\lambda_i x_i)]\exp(\mathrm{i}\omega_i t)$$
$$i = 2, 3, \tag{6b}$$

$$w_{hi}(x_i, t) = [B_i \exp(-\mathrm{i}\lambda_i x_i) + D_i \exp(-\lambda_i x_i)]\exp(\mathrm{i}\omega_i t), \quad i = 4, \tag{6c}$$

where A_i, B_i, C_i and D_i are the undetermined amplitudes at each frequency of region i.

2.3. PARTICULAR SOLUTION

Consider that an impact force F is applied at the mid-span, $x = 0$, of a beam. The force is applied via an imaginary, rigid massless joint. By not taking into account the effect of reflected wave from the boundary, the beam can be considered as an infinite beam. The free body diagram of the impacted beam is shown in Figure 2.

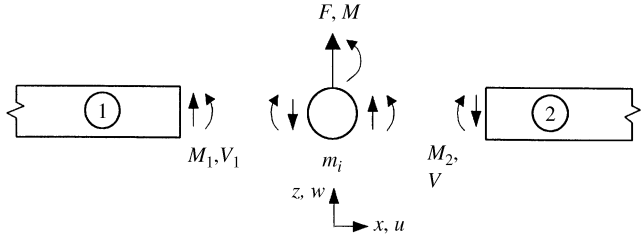

Figure 2. Free body diagram for transverse impact in beam.

The incidence transverse impact wave at $x > 0$ can be expressed as

$$w_p(x, t) = \sum A \exp(-\mathrm{i}\lambda x + \mathrm{i}\omega t) + \sum B \exp(-\lambda x + \mathrm{i}\omega t), \tag{7}$$

where A and B are undetermined coefficients, λ is the frequency parameter, depending on the dimensions and material properties of the beam, the subscript p denotes the particular solution. Since the shear force $V_1 = V_2$, the conditions at the joint should satisfy

$$\frac{\partial w}{\partial x} = 0, \tag{8}$$

$$F + 2V_2 = m_i \ddot{w} = 0. \tag{9}$$

By substituting for the moment–deflection and the moment–shear force relations in terms of displacement, the wave solution can be written as

$$w_p(x, t) = \sum \frac{-\mathrm{i}\hat{F}}{4EI\lambda^3} [\exp(-\mathrm{i}\lambda x + \mathrm{i}\omega t) - \mathrm{i}\exp(-\lambda x + \mathrm{i}\omega t)]. \tag{10}$$

The transfer function for the wave displacement is

$$\hat{G}(x, \omega) = \sum \frac{-\mathrm{i}}{4EI\lambda^3} [\exp(-\mathrm{i}\lambda x) - \mathrm{i}\exp(-\lambda x)]. \tag{11}$$

The presence of $\exp(-\lambda x)$ indicates a large contribution at $x = 0$ that decays rapidly as x increases. The transfer function depends on the reciprocal of λ^3 and, consequently, on $\omega^{3/2}$. Using the convolution theorem, the relation between force and displacement in time domain can be presented as

$$w_p(x, t) = F(x, t)^* G(x, t). \tag{12}$$

In this application, the discrete Fourier transform and its inverse are performed using the FFT-function and the IFFT-function provided by the commercial software MATLAB. Considering the fine resolutions of the data and a quick-Fourier transform algorithm for number of point equivalent with a power of two, the number of points being used is 2048. The general solution, w, of the problem is thus

$$w(x, t) = w_h + w_p, \tag{13}$$

where w_h and w_p are given by equations (6) and (12) respectively.

2.4. CONTINUITY CONDITIONS

In order to satisfy the compatibility of displacements and equilibrium of forces at the junctions between the infinite and crack regions, the conditions of continuity have to be

applied at these junctions. The continuity conditions at the junction of $x_1 = 0$ and $x_2 = 0$ are as follows:

1. Continuity of transverse displacement

$$w_1 = w_2. \tag{14}$$

2. Continuity of normal slope

$$\partial w_1/\partial x_1 = \partial w_2/\partial x_2. \tag{15}$$

The compatibility of transverse displacement and slopes between regions 1 and 3 is also automatically satisfied with the assumption of $w_2 = w_3$.

3. Continuity of shear forces

$$-EI\ \partial^3 w_1/\partial z_1^3 = -(EI_2 + EI_3)\partial^3 w_2/\partial z_2^3. \tag{16}$$

4. Continuity of bending moments

$$-EI\ \partial^2 w_1/\partial x_1^2 = -(EI_2 + EI_3)\partial^2 w_2/\partial x_2^2 + P_d(d/2). \tag{17}$$

The continuity conditions at the junction $x_2 = b$, $x_4 = 0$ are obtained by replacing w_1 and x_1 by w_4 and x_4, respectively, in equation (14)–(17).

Apart from the continuity of transverse displacement, slopes, bending moments and shear forces, an additional axial load system of equal and opposite forces on the delaminated regions is needed to maintain geometrical compatibility at the ends of these regions in the same plane. By applying the continuity of axial displacement on the junctions and neglecting the longitudinal inertia terms, the total axial force on the midplane of each of these regions can be obtained as

$$P_d = (d/2)\left(\frac{EA_{c2}A_{c3}}{b(A_{c2} + A_{c3})}\right)[\partial w_1(0)/\partial x_1 - \partial w_4(0)/\partial x_4]. \tag{18}$$

By using this expression for the axial force term, equations (14)–(17) and the corresponding equations at the second junction can be written as a set of eight simultaneous linear homogeneous equations in the eight unknown constants. The frequencies and their wave propagation mode can be obtained as the eigenvalues and eigenvectors of this equation set.

3. EXPERIMENTAL STUDY

Experiments are conducted on four aluminium beams (A1–A4) of 1000 mm length, 25·4 mm width and 4·5 mm thickness. Beam A1, which has no crack, is used as the reference beam. Cracks of 35 mm (beam A2), 45 mm (beam A3) and 55 mm (beam A4) length and at 5 mm below the surface are artificially created with a 0·25 mm-diameter milling cutter at a distance of 600 mm from the left end of the beam. The schematic diagram of the experimental set-up is shown in Figure 3.

Impact force is applied at the mid-span of the specimen in order to obtain the maximum time of observation before the incidence wave is reflected by the boundary. The impact point is maintained 100 mm away from the left edge of the crack. Impact on the beam is achieved by swinging a mechanical pendulum whose end is attached to a steel ball. The diameter of the steel ball is 15·21 mm and 9·98 mmand the angle swing is 30°. The input impact force is measured using a Kistler transducer type 8720A500 attached to the steel ball, and the response of the beam in terms of velocity on its surface is measured using

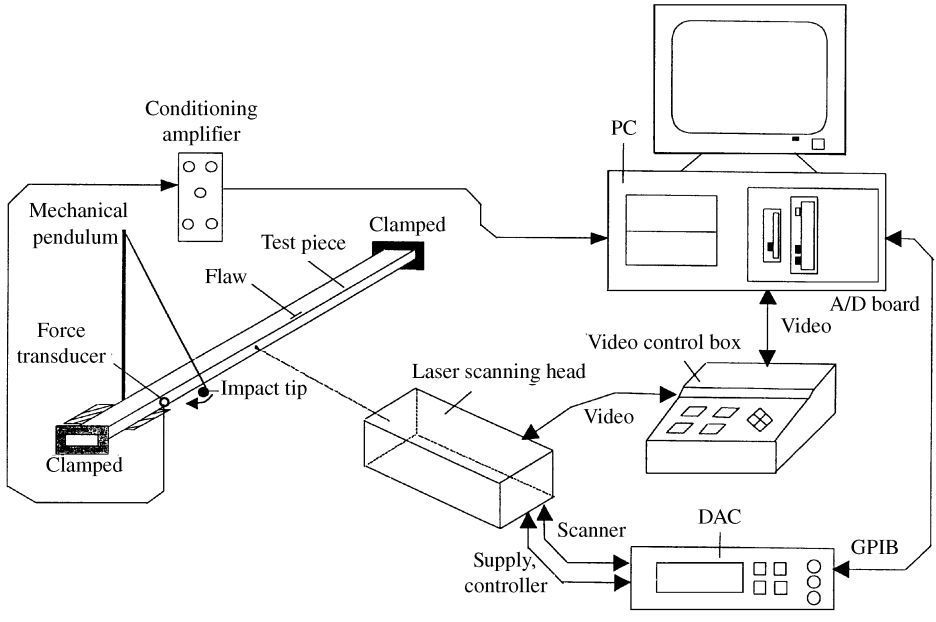

Figure 3. Schematic diagram of experimental set-up.

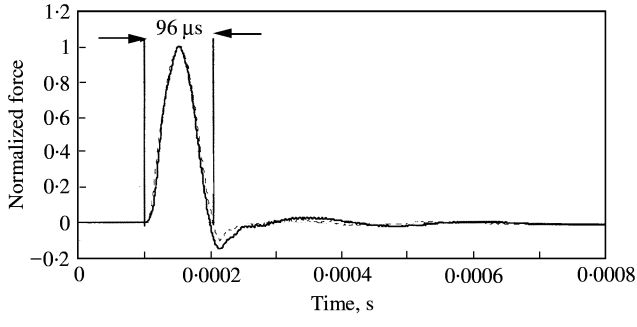

Figure 4. Time history of impact forces using steel ball of 15·21 mm diameter: ——, flawless; - - - -, flaw.

a Polytec scanning laser vibrometer. The signals from the force transducer and the laser vibrometer are then discretized and analyzed using a computer.

The fastest propagated wave in beams is the longitudinal wave that propagates at 5230 m/s. With the distance of 500 mm for the outgoing wave to travel and 500 mm distance for the reflected wave to travel, the fastest wave needs 191 μs to propagate, to be reflected and to arrive at the impact point. It means that the effective observation time should be less than 191 μs started from the instance of excitation.

The measured time history and calculated frequency domain of the excitation force generated by the 15·21 mm diameter steel ball on the flawless beam A1 and flawed beam A2 are shown in Figures 4 and 5 respectively. It is observed that the time period of the generated impact force is 96 μs. Figure 4 also shows that the shape of the recorded force time history for the flawless beam A1 is the same as that of the flawed beam A2.

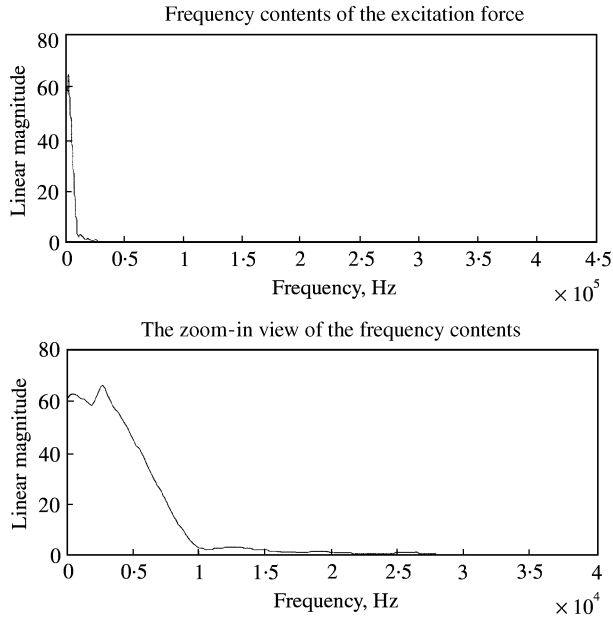

Figure 5. Frequency domain of force generated using steel ball of 15·21 mm diameter.

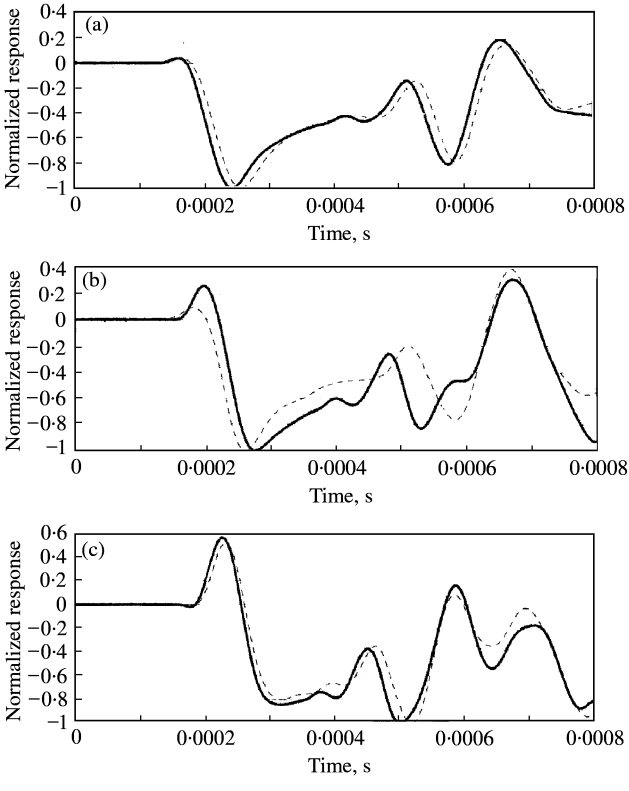

Figure 6. Time histories of beam responses under excitation from steel ball of 15·21 mm diameter. ——, flawless; - - - - -, flaw. (a) Beam response 80 mm from impact point (left-hand side of the crack); (b) Beam response 117·5 mm from impact point (above the crack); (c) Beam response 155 mm from impact point (right-hand side of the crack).

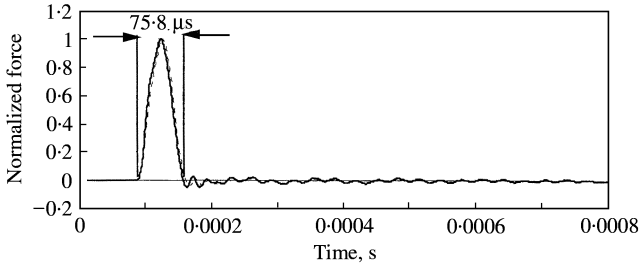

Figure 7. Time history of impact forces using steel ball of 9·98 mm diameter: ——, flawless; - - - - -, flaw.

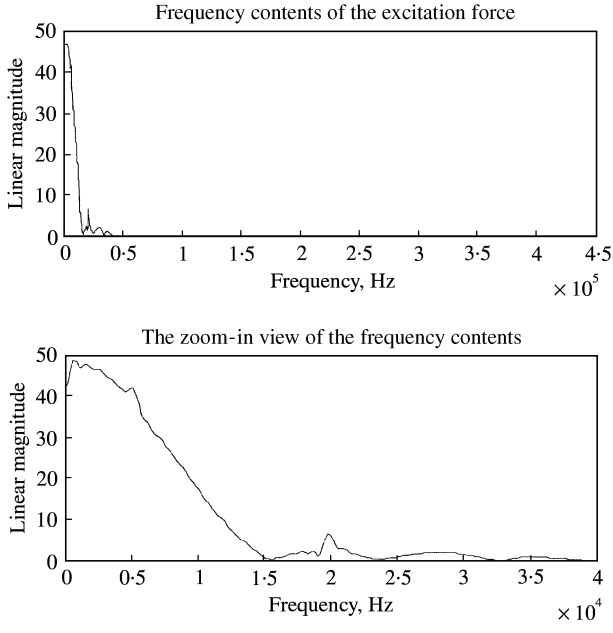

Figure 8. Frequency domain of force generated using steel ball of 9·98 mm diameter.

With the use of the 15·21 mm diameter steel ball, the time history response of the beam at points located 80, 117·5 and 135 mm from the point of impact are obtained and shown in Figure 6(a), 6(b) and 6(c) respectively. As shown in Figure 6(a) and 6(c), the responses of the flawless beam A1 and the flawed beam A2 at the left-hand and right-hand side of the crack do not indicate any significant differences. Compared with the flawless beam A1 response, flawed beam A2 response at the middle of the cracked region, as shown in Figure 6(b), indicates little differences especially at the time after 300 μs. The inconspicuous difference in response between the flawless beam A1 and the flawed beam A2 might be due to the frequency range of the excitation force being too low (Figure 5).

To overcome this limitation, one uses a smaller steel ball (9·98 mm in diameter). The measured time history and the calculated frequency domain of excitation force generated by the steel ball for the flawless beam A1 and the flawed beam A2 are shown in Figures 7 and 8 respectively. It is seen that the time period of the generated impact force is 75·8 μs. This indicates that the use of a smaller ball will generate a sharper impact force and a higher frequency range of the excitation force. Hence, the use of a smaller ball might improve the performance of the method for crack identification.

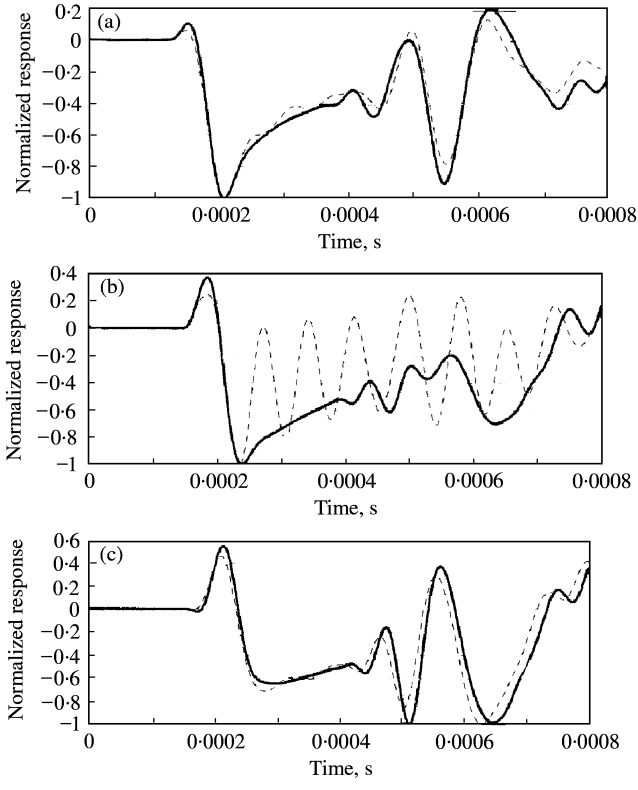

Figure 9. Time histories of beam responses under excitation from steel ball of 9·98 mm diameter. ——, flawless; - - - - -, flaw. (a) Beam response 80 mm from impact point (left-hand side of the crack); (b) Beam response 117·5 mm from impact point (above the crack); (c) Beam response 155 mm from impact point (right-hand side of the crack).

With the use of the 9·98 mm diameter steel ball, the time history of beam response at points located 80, 117·5 and 135 mm from the point of impact are shown in Figure 9(a), 9(b) and 9(c) respectively. The results in Figures 6 and 9 also indicate that the beam response is dispersive. As shown in Figure 9(a) and 9(c), the presence of the crack can generate additional small oscillations to the beam responses at the left-hand and the right-hand side of the crack after reaching the minimum point of the response at 208 and 274 μs respectively. Responses at the middle of the cracked region, as shown in Figure 9(b), indicate a very significant difference between the flawless and the flawed beams. The response of the flawed beam A2 shows a tremendous oscillation when the incidence wave propagates through the cracked region. These evidences are then used as a tool to identify the presence of the crack.

4. COMPARISON STUDY

The transfer function of the wave displacement, $\hat{G}$, calculated using the beam model for wave propagation, is shown in Figure 10. Relating the transfer function for wave displacement with the frequency domain of the excitation force indicates that the force generated with the use of the smaller ball may cover a wide frequency range of the transfer function; hence the ability to detect cracks is enhanced.

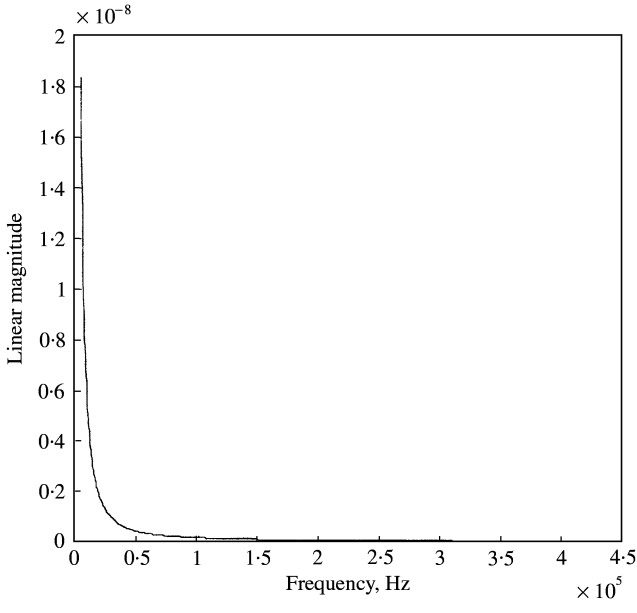

Figure 10. Transfer function of the wave displacement, $\hat{G}$.

Numerical and experimental time history of flawless beam A1 responses at points located 80, 117·5 and 155 mm from the point of impact are presented in Figure 11, the numerical responses being calculated using beam model and FEM and the experimental responses being taken from laser measurement. The flawless beam A1 responses calculated using the beam model are presented by the particular solution described in equation (12). It shows that the results of the present beam model agree reasonably well with the FEM and experimental results until the wave reflected from the boundary interferes with the incidence wave. As the FEM model is developed based on clamp–clamp boundary condition, its response indicates oscillation after the incidence wave is reflected by the boundary.

The interference between the reflected and incidence waves is indicated by the oscillation on the beam responses beyond 400 μs. These oscillations do not appear in the beam model responses due to the assumption of an infinite beam; in which case the incidence wave will not be reflected back by the boundary (the end of the beam). In all the cases, the experimental results match the beam model results better than the FEM results. As shown in Figure 11, a smooth beam response with no oscillation before interference between incidence and reflected waves occurs can be used as an indication of a flawless beam.

Numerical and experimental time history of flawed beam A2 responses at points located 80, 117·5 and 155 mm from the point of impact are shown in Figure 12. Results obtained from the present beam model agree reasonably well with both the FEM and the experimental results for flawed beams, even though interference of the incidence and reflected waves do cause differences between the beam model results and experiments. Besides the oscillation due to interferences, there is a small oscillation on the beam response at the left-hand and the right-hand side of the crack, as shown in Figure 12(a) and 12(c). The oscillation becomes more prominent when the response is calculated at the middle of the crack as shown in Figure 12(b). These results can be used as a clear indication of the presence of a crack.

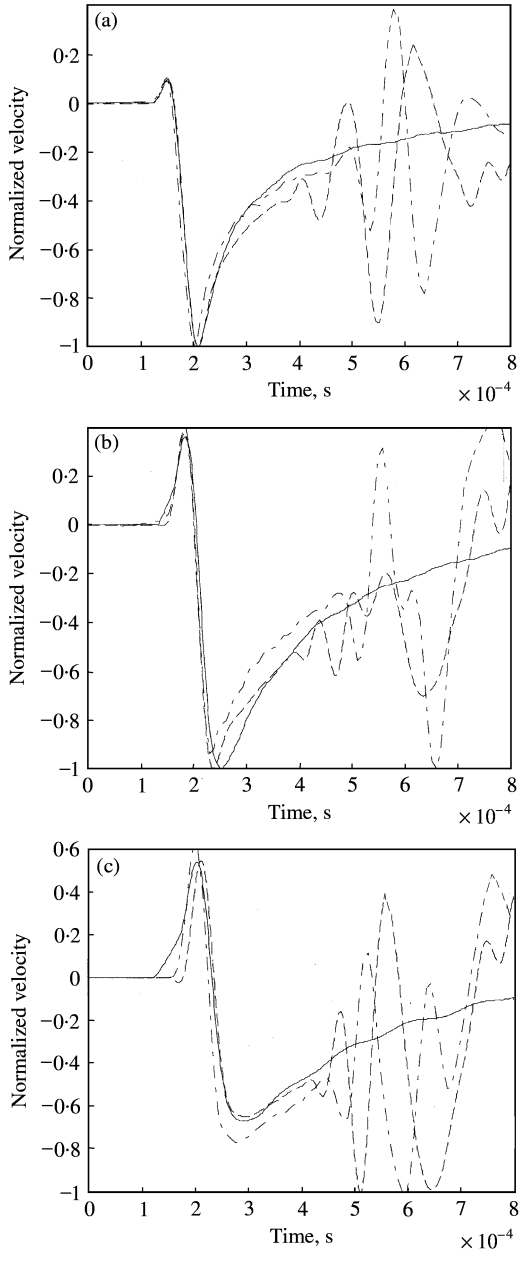

Figure 11. Comparison study of time history of flawless beam response from beam model, FEM and laser measurement. ——, beam model; – – –, FEM; – – – –, laser. (a) Time history of flawless beam response 80 mm from excitation point; (b) Time history of flawless beam response 117·5 mm from excitation point; (c) Time history of flawless beam response 155 mm from excitation point.

5. INVERSE CRACK DETERMINATION USING BEAM MODEL AND MLP

The comparison studies indicate that the beam model results agree reasonably well with the experiment. Their results indicate that time domain response is perturbed due to the presence of crack, inferring that time-domain response may be used to locate and size

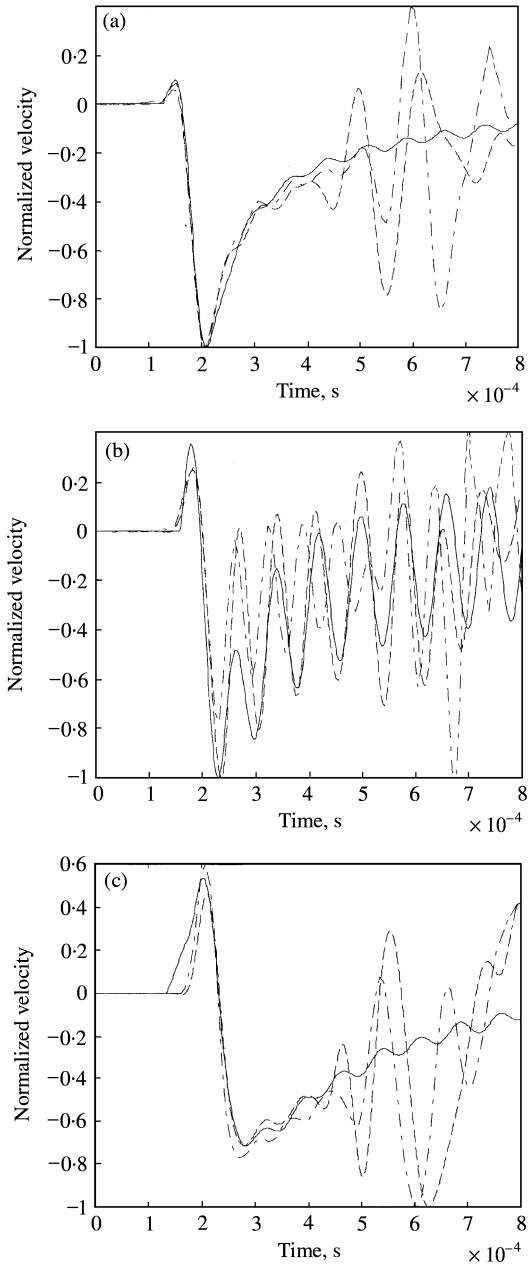

Figure 12. Comparison study of time history of flawed beam response from beam model, FEM and laser measurement. ——, beam model; – – – –, FEM; – – -, laser. (a) Time history of flawed beam response 80 mm from excitation point; (b) Time history of flawed beam response 117·5 mm from excitation point; (c) Time history of flawed beam response 155 mm from excitation point.

delaminations in beams. After extensive comparison studies [17] between the beam model and experimental results; the beam model is then used together with the adaptive MLP for inverse identification of crack parameters in the beams.

Figure 13 illustrates the MLP network for detecting crack in beam. It includes (1) initial training of the MLP model using the elaborate training data, and (2) reconstruction of

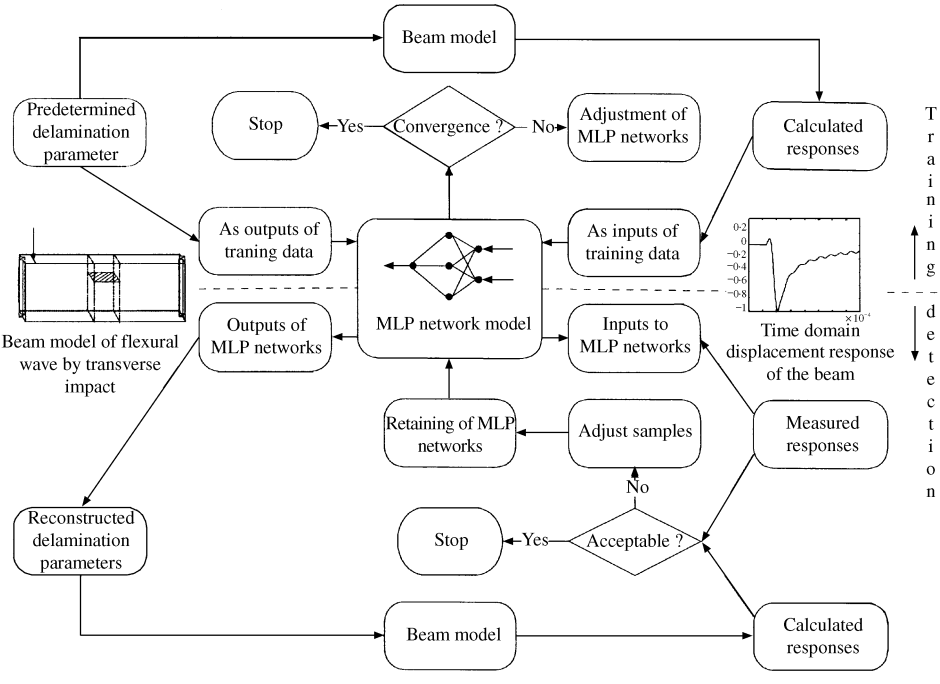

Figure 13. Strategy for training and application of MLP network.

TABLE 1

Discrete values of crack parameters in time domain analysis

Location, d_f	$20/H$	$-17{\cdot}5/H$	$-55/H$
Depth, d_c	$5/H$	$20/H$	
Length, a_c	$35/H$	$45/H$	$55/H$

Note. $H = 4{\cdot}5$ (unit: mm).

the crack using the trained MLP model by inputting the experimental time-domain displacement response of the beam. If the displacement response calculated from the reconstructed crack parameters compared with the experimental data do not satisfy the Euclidean criterion that will be described later, the MLP networks will be retrained in order to obtain another set of improved delamination parameters. More details about the MLP and its parameters are described by Xu *et al.* [18], Mahmoud and Kiefa [19], Rhim and Lee [20].

The input for MLP is taken from beam model responses of 40 points starting from the first peak response until the response at 350 μs. This training data correspond with the displacement response that has not been interfered by the reflected wave, hence the good correlation between beam model results and experiment can be well maintained. The number of neurons in the outer layer of MLP is 3 that represent the reconstructed crack parameters $\mathbf{P} = \{d_f, d_c, a_c \cdot \mathrm{a}_c$ and d_c denote the length of the crack and its depth from the upper surface of the beam, d_f denotes the distance between the measurement point and the left-hand edge of the crack (see Figure 1). Using correlation analysis between the output of

TABLE 2

The configuration of time domain training data for MLP

Location, d_f		Death, d_c		Length, a_c	
Actual ($\times$ 1/H)	Normalized	Actual ($\times$1/H)	Normalized	Actual ($\times$ 1/H)	Normalized
20·0	0·98	0·00	0·00	0·00	0·00
− 55·00	0·07	0·00	0·00	0·00	0·00
− 17·50	0·52	5·00	0·23	35·00	0·58
− 55·00	0·07	5·00	0·23	35·00	0·58
20·00	0·98	20·00	0·91	35·00	0·58
− 55·00	0·07	20·00	0·91	35·00	0·58
20·00	0·98	5·00	0·23	45·00	0·74
− 17·50	0·52	5·00	0·23	45·00	0·74
− 55·00	0·07	5·00	0·23	45·00	0·74
20·00	0·98	20·00	0·91	45·00	0·74
− 55·00	0·07	20·00	0·91	45·00	0·74
20·00	0·98	5·00	0·23	55·00	0·91
− 17·50	0·52	5·00	0·23	55·00	0·91
20·00	0·98	20·00	0·91	55·00	0·91
− 17·50	0·52	20·00	0·91	55·00	0·91

neurons in the hidden layers, the number of neurons are assigned to be 24 and 9 for the 1st and 2nd hidden layers respectively. The discrete values of crack parameters are presented in Table 1.

Considering the completeness of the sample space, 15 combinations of crack parameters are used as training data for the MLP networks. Over the training process, the values learning rate, $\eta = 2{\cdot}0$ and momentum rate, $\alpha = 0{\cdot}5$ are used in the modified back propagation algorithm. The actual and normalized training data of crack parameters are presented in Table 2. For the initial training process, the optimized MLP networks have satisfied the given convergence criterion after 14 751 iterations.

After the initial training of the MLP model, reconstruction of delamination parameters begins by inputting the experimental displacement response $\mathbf{U}_m(x, z)$ measured from the scanning laser vibrometer into the MLP network. The output of the MLP model would be the reconstructed crack parameters $\mathbf{P}_r$. These reconstructed parameters are then inputted to the beam model to produce a set of calculated displacement response $\mathbf{U}_c(x, y)$. Comparison between the reconstructed displacement responses $\mathbf{U}_c(x, y)$. Comparison between the reconstructed displacement responses $\mathbf{U}_c$ and the measured ones $\mathbf{U}_m$ are calculated using Euclidean criterion as follows:

$$Err = \| \mathbf{U}_c - \mathbf{U}_m \|_2 . \tag{19}$$

If the value of *Err* exceeds the permissible error $E_c = 20\%$, then the MLP network will be retrained using the adjusted training samples that contain $\mathbf{U}_c(x, y)$ and $\mathbf{P}_r$. The retrained MLP model is then used to reconstruct the crack parameters again by inputting the measured $\mathbf{U}_m(x, z)$. This procedure would be repeated until $Err \leqslant Ec$, implying that the reconstructed crack parameters would be able to produce the displacement responses that are sufficiently close to the measured ones when inputted to the beam model.

As the results of the first training process, in general, the calculated delamination parameters compared to the measured ones still do not satisfy the given Euclidean criterion. The MLP networks are then retrained with the adjusted sample sets for reconstructing the

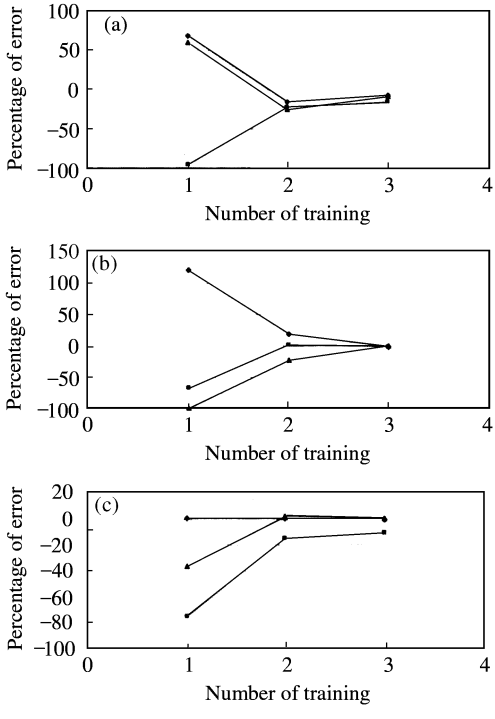

Figure 14. The converging of cracks parameters error reconstructed by the MLP. —◆—, location (df), —■—, depth (dc); —▲—, length (ac). (a) Isotropic beam case of $d_f = -17{\cdot}5/H$, $d_c = 5/H$, $a_c = 35/H$; (b) Isotropic beam case of $d_f = -17{\cdot}5/H$, $d_c = 20/H$, $a_c = 45/H$; (c) Isotropic beam case of $d_f = -20/H$, $d_c = 5/H$, $a_c = 55/H$.

TABLE 3

Comparison between the actual and reconstructed crack parameters

	Location, d_f		Depth, d_c		Length, a_c		Percentage of error		
No.	Measured	Calculated	Measured	Calculated	Measured	Calculated	Location	Depth	Length
1	20·00	19·91	0·00	0·04	0·00	0·07	− 0·44	0·00	0·00
2	− 17·50	− 17·30	0·00	0·00	0·00	0·01	− 0·13	0·00	0·00
3	− 55·00	− 54·58	0·00	0·00	0·00	0·01	− 0·75	0·00	0·00
4	20·00	20·22	5·00	4·11	35·00	28·44	1·09	− 17·12	− 18·76
5	− 17·50	− 16·36	5·00	4·20	35·00	31·91	− 6·50	− 15·92	− 8·84
6	− 55·00	− 54·41	5·00	4·38	35·00	35·60	− 1·07	− 12·40	1·73
7	20·00	20·10	20·00	17·73	35·00	34·52	0·51	− 11·33	− 1·38
8	− 17·50	− 16·22	20·00	19·66	35·00	33·49	− 7·30	− 1·70	− 4·32
9	− 55·00	− 55·22	20·00	20·39	35·00	39·03	0·40	1·95	11·53
10	20·00	20·12	5·00	4·11	45·00	46·83	0·59	− 17·72	4·06
11	− 17·50	− 18·22	5·00	4·63	45·00	48·97	4·11	− 7·34	8·82
12	− 55·00	− 54·72	5·00	4·18	45·00	46·16	− 0·51	− 16·40	2·57
13	20·00	20·18	20·00	16·50	45·00	45·31	0·88	− 17·50	0·70
14	− 17·50	− 17·20	20·00	19·75	45·00	45·01	− 1·69	− 1·23	0·03
15	− 55·00	− 55·23	20·00	20·15	45·00	45·39	0·42	0·73	0·87
16	20·00	19·96	5·00	4·49	55·00	55·27	− 0·19	− 10·28	0·49
17	− 17·50	− 17·83	5·00	5·35	55·00	56·94	1·89	6·96	3·52
18	− 55·00	− 55·10	5·00	5·93	55·00	54·68	0·18	18·67	− 0·58
19	20·00	20·16	20·00	16·12	55·00	55·71	0·80	− 19·40	1·29
20	− 17·50	− 17·48	20·00	20·02	55·00	54·94	− 0·14	0·10	− 0·11
21	− 55·00	− 54·89	20·00	19·85	55·00	54·88	− 0·20	− 0·76	− 0·22

crack parameters. For the second and third training, the optimized MLP networks have satisfied the given convergence criterion after 12 929 and 10 097 iterations respectively.

Figure 14 shows three samples of convergence processes of these crack parameters reconstructed from the MLP networks. These results indicate that the error of the reconstructed crack parameters decreases significantly with the progress of the retraining process.

The total comparison results between the actual and reconstructed delamination parameters for 21 testing data are presented in Table 3. It is shown that the beam model of wave propagation and MLP networks can correctly determine the location, the depth and the length of crack over a wide range of crack parameters contained in the cracked aluminium beam. For these cases, the percentage of errors between the measured and calculated delamination parameters are less than $-19{\cdot}4\%$. High percentage errors are found in the case of deep crack because the beam model of wave propagation is applied well only on a slender beam in which the effects of rotary inertia and shear deformation are not taken into consideration. Hence, the application of this model for deep crack may contribute more error to the prediction of crack parameters.

6. CONCLUSIONS

Four studies are carried out in this paper: (1) analytical study using a beam model for wave propagation in a flawless and a flawed beam; (2) experimental study; (3) comparison study between theoretical and experimental results and; (4) inverse crack determination using beam model and MLP. The beam model results correlate well with the experiment and FEM results. The results have also indicated that the presence of flaw may reflect or scatter the incidence transverse wave and generate a very significant change in the pattern of the beam response, thereby enabling detection of flaws in a beam.

The effectiveness of this method is greatly affected by frequency range of the impact force. At high-frequency impact, a pronounced change in the beam response is observed; hence the presence of a flaw in the beam is clearly revealed.

The beam model of wave propagation in time domain and MLP networks have also been applied and can correctly determine the location, the depth and the length of crack over a wide range of crack parameters contained in the cracked aluminium beam. These results indicate that this method is accurate and efficient for quantifying the size and location of the cracks in beams that are not too deep from the surface.

REFERENCES

1. P. CAWLEY 1984 *NDT International* **17**, 59–65. The impedance method of non-destructive inspection.
2. P. F. RIZOS, N. ASPRAGATHOS and A. D. DIMAROGONAS 1990 *Journal of Sound and Vibration* **138**, 381–388. Identification of crack location and magnitude in a cantilever beam from the vibration modes.
3. Y. NARKIS 1994 *Journal of Sound and Vibration* **172**, 549–558. Identification of crack location in vibrating simply supported beams.
4. L. S. PENN, J. R. JUMP, M. J. GREENFIELD and G. E. BLANDFORD 1999 *Journal of Composite Material* **33**, 54–72. Use of the free-free vibration spectrum to detect delamination in thick composites.
5. W. T. SPRINGER, K. L. LAWRENCE and T. J. LAWLEY 1988 *Experimental Mechanics* **45**, 34–37. Damage assessment based on the structural frequency-response function.
6. C. H. ROCHE and M. L. ACCORSI 1998 *Finite Element Analysis* **31**, 165–177. A new finite element for global modelling of delaminations in laminated beams.

7. P. M. MUJUMDAR and S. SURYANARAYAN 1988 *Journal of Sound and Vibration* **125**, 441–461. Flexural vibrations of beams with delaminations.
8. G. R. LIU and J. D. ACHENBACH 1995 *American Society of Mechanical Engineers Journal of Applied Mechanics* **62**, 607–613. Strip element method to analyze scattering by cracks in anisotropic laminated plates.
9. G. R. LIU, K. Y. LAM and T. A. OHYOSHI 1997 *Composites and* **28B**, 667–677. Technique for analyzing elastodynamic responses of anisotropic laminated plates to line loads.
10. J. F. DOYLE 1995 *Experimental Mechanics* **52**, 272–280. Determining the size and location of transverse cracks in beams.
11. J. F. DOYLE and S. KAMLE 1985 *Experimental Mechanics* **52**, 669–673. An experimental study of the reflection and transmission of flexural waves at discontinuities.
12. J. F. DOYLE and S. KAMLE 1987 *Journal of Applied Mechanics T-ASME* **54**, 136–140. An experimental study of the reflection and transmission of flexural waves at an arbitrary T-joint.
13. J. F. DOYLE 1987 *Journal of Sound and Vibration* **118**, 441–448. Experimentally determining the contact force during the transverse impact of an orthotopic plate.
14. J. F. DOYLE 1987 *Experimental Mechanics* **44**, 68–72. Determining the contact force during the transverse impact of plates.
15. J. F. DOYLE 1987 *Experimental Mechanics* **44**, 229–233. An experimental method for determining the location and time of initiation of an unknown dispersing pulse.
16. C. L. CHEE 2000 Finite element simulation of wave scattering by flaws in beams. *B.Eng. Thesis*, National University of Singapore.
17. S. I. ISHAK 2000 The use of flexural waves for non-destructive evaluation of structures. *Ph.D. Thesis*, National University of Singapore.
18. Y. G. XU, G. R. LIU, Z. P. WU and X. M. HUANG 2000 *International Journal of Solids Structure*. Adaptive multilayer perception networks for detection of cracks in anisotropic laminated plates. (accepted).
19. M. A. MAHMOUD and M. A. A. KIEFA 1999 *NDT&E International* **32**, 91–99. Neural network solution of the inverse vibration problem.
20. J. RHIM and S. W. LEE 1995 *Computational Mechanics* **16**, 437–443. Neural networks approach for damage detection and identification of structures.
21. O. ERSOY 1997 *Fourier-Related Transforms, Fast Algorithms, Fast Algorithms and Applications*, 44–45. Englewood Cliffs, NJ: Prentice-Hall Inc.
22. R. D. KELLY and G. RICHMAN 1969 *Principles and Techniques of Shock Data Analysis*. The Shock and Vibration Information Center, U.S. Department of Defense.
23. V. I. BABITSKY 1998 *Theory of Vibro-Impact Systems and Applications*. Berlin: Springer-Verlag.